4.4 SIMULATION OF THE GABLS STABLE BOUNDARY LAYER INTERCOMPARISON CASE USING ONE-DIMENSIONAL TURBULENCE

Alan R. Kerstein and Scott Wunsch
Combustion Research Facility, Sandia National Laboratories, Livermore, California

1 INTRODUCTION

One-Dimensional Turbulence (ODT) is a turbulence simulation model formulated on a one-dimensional (1D) spatial domain. In an ABL context, it is nominally a single-column model (SCM) representing the vertical structure of the atmosphere, but functionally it has a greater resemblance to large-eddy simulation (LES) in some respects.

Specifically, ODT is a method for simulating, on an unsteady time-resolved basis, the time evolution of profiles of velocity and other fluid properties that one might measure along a one-dimensional (1D) line of sight through a 3D turbulent flow. In the 1D dynamical process defined by the ODT model, the effects of turbulent 3D eddies associated with real fluid flow are captured by 1D fluid-element rearrangement events that occur over a range of length scales with frequencies that depend on event length scales and instantaneous flow structure.

ODT is an outgrowth of the linear-eddy model (LEM), in which fluid motions are prescribed without explicit introduction of a velocity field or dependence on the instantaneous flow (Kerstein, 1991). The first ODT formulation (Kerstein, 1999) involved simulation of a single velocity component evolving on a line. A more recent formulation (Kerstein et al., 2001) introduced the evolution of the three-component velocity vector on the 1D domain.

The formulation presented here is the first to combine this vector-velocity formulation with a compatible treatment of buoyancy effects (Wunsch and Kerstein, 2001) and other features needed to simulate the stable boundary layer in conformance with the specifications of the GABLS intercomparison (Cuxart et al., 2004). This paper is a companion to that intercomparison. Accordingly, description of the GABLS field study and the specifications of the intercomparison are not repeated here. The present goal is to introduce the ODT methodology to the atmospheric sciences community in the context of an application to an atmospheric flow regime of current interest.

In previous ODT applications to laboratory-scale flows (but not in the present application), the 1D domain resolved molecular-transport processes (viscosity, heat transport, mass transport, etc.). Turbulent transport, which is usually modeled as a diffusive process, is represented in ODT by a random sequence of rearrangements (mathematically, mappings) applied to randomly selected intervals of the 1D domain. These rearrangements may be viewed as the model analog of turbulent eddies, and are therefore termed eddies or eddy events.

The mapping that represents a turbulent eddy is defined so as to emulate the key attributes of turbulent eddies: overturning motion and compression that amplifies property gradients. It may be viewed as an idealization of the effect of a notional turbulent eddy on property profiles along a 1D line of sight.

The times of occurrence, locations, and spatial extents of eddy events in ODT are randomly sampled. The physics governing the spatiotemporal structure of turbulence is incorporated through the mathematical relations that determine the likelihood of particular eddy events as a function of the instantaneous flow state. These relations are based on familiar, well established mixing-length phenomenology. This application of mixing-length concepts is closer in principle to the underlying physics than mixing-length applications to formulations involving spatial, temporal, or ensemble averaging. Though the mixing-length relations used in ODT are parameterizations, their adherence to the physics governing local, time-resolved evolution results in a particularly simple, robust formulation involving minimal parameter adjustment. Numerous applications supporting this characterization have been reported in the literature (Kerstein, 1999; Kerstein et al., 2001; Schmidt et al., 2003; Wunsch and Kerstein, 2001).

In Sec. 2, the ODT modeling concept is motivated in an atmospheric flow context by comparing it to Stull's (1988) transilient model of the ABL. The ODT formulation applied here to

the GABLS intercomparison case is described in Sec. 3. The description is intended to summarize the present formulation with emphasis on differences from previous formulations. A new feature is that molecular-transport processes are not resolved in this application. Therefore the transport coefficients in the under-resolved ODT simulations represent the transport associated with unresolved subgrid motions, i.e., they are eddy-viscosity and eddy-diffusivity coefficients. In this regard, the formulation is functionally analogous to LES, with the important difference that advection in ODT is based on a model designed for application in one spatial dimension.

Two different methods are used to determine these coefficients. In one method, viscosity is assigned a fixed value that phenomenologically represents near-surface roughness effects. This assignment, an assumed value of the turbulent Prandtl number, and assignment of another parameter that controls the von Karman constant, are the only empirical inputs other than the physical setup specified for the intercomparison. This method requires resolution of the roughness length. The other method, which is implemented at lower spatial resolution, involves a variable eddy viscosity determined by the local mesh-resolved flow, as in multi-dimensional large-eddy simulation (LES). The roughness length is not an input to this formulation, but the formulation involves two free parameters.

The results obtained from application of these two alternative formulations are presented and discussed in Sec. 4. When the less costly variable-viscosity approach is run at typical LES resolution (64 cells spanning 400 m), it captures much of the relevant physics but is found to have some significant limitations. Prospects for improvement of the low-resolution methodology, as well as prospects for use of ODT as a near-surface subgrid closure framework for general circulation models (GCMs), are assessed.

2 THE ODT MODELING CONCEPT

2.1 Comparison to the Transilient Model

The ODT modeling concept is introduced in an atmospheric context by comparing it to Stull's (1988) transilient model of the ABL. The relevant features of Stull's approach are as follows:

1. Structurally, the transilient model is a single-column model (i.e., a vertical column of control volumes).
2. The model evolves by fluxing fluid from cell to cell.
3. The unique feature is that this fluxing is not limited to nearest-neighbor transfers. A given cell may in principle transfer fluid to any other cell.
4. For every possible pair of origin and destination cells, the fluid transfer rate is parameterized by a turbulent kinetic energy (TKE) equation involving mechanical production, buoyant production, and dissipation terms. The intent is to quantify the transport by eddy motions that transfer fluid from the origin cell to the destination cell.

The transilient model and ODT are analogous in many respects, but there are four key differences between the two approaches:

1. The transilient model is based on ensemble averaging, which smooths fine-scale fluctuations, but ODT is implemented as an unsteady simulation of individual flow realizations; each realization exhibits variability at all resolved length and time scales.
2. Transilient fluxing is a mixing process that subsumes both eddy transport and molecular mixing. In ODT, resolved- scale eddy transport is implemented by performing permutations of the vertical ordering of cells, involving no fluid mixing. These permutations are instantaneous events, in contrast to the nominally continuous time evolution of the transilient model (although the numerical time step is in some respects a physical parameter in the transilient model). An additional, purely local (nearest-neighbor) continuous-time fluxing process is introduced in ODT to represent cell-scale eddy transport and mixing. This approach provides a clear distinction between advective processes, operating over a range of resolved scales, and diffusional and microphysical processes, which need to be parameterized only at intra- cell length scales (or they can be fully resolved in applications to laboratory-scale flows, and in fact

have been fully resolved in all ODT applications to date).

3. Each cell of the ODT columnar domain carries three velocity components as well as thermodynamic properties. These velocities govern mechanical production in the ODT analog of the transilient TKE equation. Mechanical production, which is thus an internal model process rather than an extrinsic parameterization, is one of the inputs controlling the sequence of permutation events. ODT velocity profiles evolve as a result of vertical permutations of cells, diffusive fluxing of momentum between nearest-neighbor cells, and an additional mechanism reflecting the effects of body forces (Secs. 2.2, 3.3, and 3.4). This additional mechanism coincides with the permutation event. The processes collectively associated with the event constitute an 'eddy event,' the ODT representation of an individual turbulent eddy.

4. The velocity profiles are thus affected by, and indirectly control (through their influence on the sequence of permutation events), the ODT advection process, but they do not advect fluid directly. Operationally, they are auxiliary variables within ODT, but they have the additional attribute that they are the ODT representation of the physical velocity field. Therefore velocity statistics are based on the ODT velocity profiles, with the important caveat that vertical advective fluxes, which are rates of transport, are based on the actual ODT vertical advective transport mechanism (eddy events). For example, $\langle u'w' \rangle$ is evaluated by monitoring the vertical transfers of the u velocity by eddy events during the ODT simulation (actually an ensemble of ODT simulations, unless the flow is statistically steady). Detailed prescriptions for extraction of velocity statistics from ODT simulations are available (Kerstein, 1999; Kerstein et al., 2001).

Next, the numerical implementation of a simulated ODT realization is outlined heuristically. Formal mathematical specification of the model is provided in Sec. 3.

2.2 Outline of Numerical Implementation

During a simulated ODT realization, local fluxing processes are implemented using a conventional time-stepping procedure. This time advancement is punctuated by the occurrence of eddy events. Each event results in a modified flow state that is the initial condition for further time advancement of the local fluxing processes. Though the two processes affect each other, reflecting relevant physical couplings, they are algorithmically distinct so they are explained separately.

Local fluxing is implemented in a purely conventional manner. In the formulation introduced here, fluxing of velocity represents cell-scale eddy viscosity, and fluxing of thermodynamic properties represents cell-scale eddy diffusivity and mixing. Concurrent with fluxing, any parameterized intra-cell microphysics that is included in the model is updated. (None is included in the present formulation.)

An eddy event involves three steps. First, an eddy, defined by the range of cells that is affected, must be selected. The next step is execution of the prescribed vertical reordering of the cells in the selected range, implemented as adiabatic fluid-parcel translations. The third step is an operation that is distinct from cell permutation, yet intimately tied to it. Namely, vertical profiles of velocity components within the selected range are modified so as to increase or decrease the total kinetic energy, while conserving momentum. This step is required primarily because the reordering generally changes the buoyant potential energy, requiring an equal-and-opposite change of kinetic energy to reflect the work done by the eddy (stable case) or the energy transferred to the eddy (unstable case). A secondary consideration is the redistribution of kinetic energy among velocity components by thereturn-to-isotropy mechanism (Pope, 2000).

The vertical reordering is explained here in Stull's (1988) mathematical framework. Stull implements the fluxing of fluid between cells of the vertical column using a matrix c_{ij} that represents the fraction of cell-j fluid transferred to cell i during a particular fluxing operation. To implement a permutation with no fluid mixing, all matrix elements must be 0 or 1. For a permutation within a designated range $Z \le j \le Z + 3S - 1$, c_{ij} is a permutation matrix of assigned form (see below) for i and j in the range $[Z, Z + 3S - 1]$,

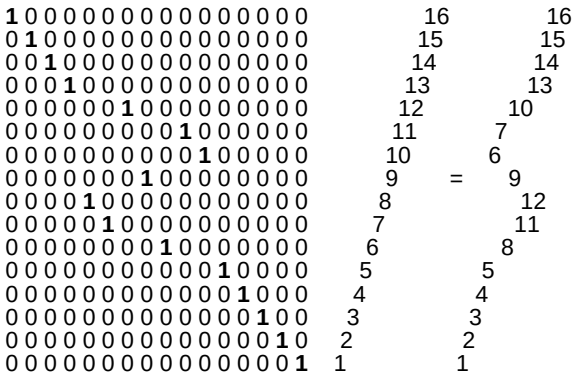

Figure 1: Application of a reordering, with $Z = 5$ and $S = 3$, to a 16-element column vector with vertically increasing cell indices. For clarity, unity matrix elements are boldface and cells are shifted horizontally in proportion to their index values. The shifts are intended to suggest the vertical profile of an adiabatically invariant property.

where Z and S are integers and $3S$ is the number of cells affected by the permutation. Outside this range, c_{ij} is unity along the diagonal, otherwise zero. For reasons discussed in Sec. 3.3, and in further detail by Kerstein (1991), the $3S \times 3S$ sub-matrix c_{ij} for i and j ranging from Z to $Z + 3S - 1$ is defined by setting matrix elements equal to unity for $(i-Z+1, j-Z+1) = (1,1), (2,4), (3,7), \ldots, (S, 3S-2), (S+1, 3S-1), (S+2, 3S-4), \ldots, (2S, 2), (2S+1, 3), (2S+2, 6), \ldots, (3S, 3S)$, and setting all other elements of the sub-matrix to zero.

An example is shown in Figure 1. The shape of the permuted profile indicates that the permutation increases property gradients and introduces an overturn (sign change of gradient) in the central third of the eddy. These features are reminiscent of the effect of an eddy turnover on a vertical sounding through 3D turbulence; the permutation is defined so as to emulate this effect.

The key physical content of the model is a sampling procedure that governs the time sequence of eddy events and the choice of the parameters Z and S that determine the range of a given event. The physical considerations on which the procedure is based are analogous to those on which Stull's procedure for evaluating the transfer coefficients c_{ij} are based. Details are provided in Sec. 3.4.

The cell-reordering process has important thermodynamic consequences when applied to a vertical fluid column in a gravitational field due to the pressure change associated with vertical displacement. This effect is incorporated by representing the thermodynamic state by a variable that is unchanged by adiabatic vertical displacments. For the GABLS case, which omits moist processes, potential temperature is used.

As in LES, the unsteady nature of the model accommodates departures from thermodynamic equilibrium due to finite-rate processes such as atmospheric chemistry and aerosol microphysics. Non-equilibrium effects will be addressed in future investigations of microphysical couplings to multi-scale dynamics. A previous LEM application to the non-equilibrium evolution of droplet spectra in cumulus clouds (Su et al., 1998) demonstrated the benefits of using the LEM/ODT concept to simulate non-equilibrium microphysics coupled to multi-scale dynamics.

3 MODEL FORMULATION

3.1 Modeling Approach

A formal mathematical statement of the modeling approach outlined in Sec. 2.2 is presented. The introductory description outlined the discrete numerical implementation. Henceforth, space and time variables are continuous unless stated otherwise.

The ODT formulation utilized here simulates the time evolution of velocity components u, v, and w and potential temperature θ defined on a one-dimensional domain corresponding to the vertical coordinate z. This evolution involves two processes: (1) a sequence of eddy events, which are instantaneous transformations that represent turbulent stirring, and (2) intervening time advancement of conventional form. Each eddy event may be interpreted as the model analog of an individual turbulent eddy. The location, length scale, and frequency of eddy events are determined by a stochastic model explained in Sec. 3.4.

3.2 Time Advancement

During the time interval between each eddy event and its successor, the time evolution of property profiles is governed by the equations

$$\left(\partial_t - \nu\partial_z^2\right) u(z,t) = f\left(v(z,t) - V_g\right) \qquad (1)$$

$$\left(\partial_t - \nu\partial_z^2\right) v(z,t) = -f\left(u(z,t) - U_g\right) \quad (2)$$

$$\left(\partial_t - \nu\partial_z^2\right) w(z,t) = 0 \quad (3)$$

$$\left(\partial_t - \gamma\partial_z^2\right) \theta(z,t) = 0. \quad (4)$$

Here ν is viscosity, γ is thermal diffusivity, f is the Coriolis parameter, and U_g and V_g are specified geostrophic winds. These equations are solved within a closed domain of height H. Boundary conditions applied to the velocity at the surface are $u(z=0) = v(z=0) = w(z=0) = 0$ and at the top are $u(z=H) = U_g$, $v(z=H) = V_g$, and $w(z=H) = 0$. For the intercomparison case, the specified surface potential temperature is $\theta(z=0,t) = \theta_0 - \dot{\theta}_g t$. The potential temperature at $z = H$ is fixed at all times at $\theta(z=H) = \theta_0 + \Delta\theta$. Parameter values, spatial resolution, and initial profiles for the intercomparison case are discussed in Secs. 3.5, 3.6, and 4.

Due to the inability to resolve molecular transport in this ODT application, ν and γ represent transport by unresolved advection, as in LES, rather than molecular transport. Two alternative methods for determining ν and γ in this context are described in Secs. 3.5 and 3.6, respectively.

3.3 Eddy Definition

Each eddy event consists of two mathematical operations. One is a measure-preserving map representing the fluid displacements associated with a notional turbulent eddy. The other is a modification of the velocity profiles in order to implement pressure-induced energy redistribution among velocity components and net kinetic-energy gain or loss due to equal-and-opposite changes of the gravitational potential energy. These operations are represented symbolically as

$$\begin{array}{lcl} \theta(z) & \rightarrow & \theta(M(z)) \\ u(z) & \rightarrow & u(M(z)) + c_u K(z) \\ v(z) & \rightarrow & v(M(z)) + c_v K(z) \\ w(z) & \rightarrow & w(M(z)) + c_w K(z). \end{array} \quad (5)$$

According to this prescription, fluid at location $M(z)$ is moved to location z by the mapping operation, thus defining the map in terms of its inverse $M(z)$. This mapping is applied to all fluid properties. The additive term $c_s K(z)$, where $s = u$, v, or w, affects only the velocity components. It implements the aforementioned kinetic-energy changes. Potential-energy change is inherent in the mapping-induced vertical redistribution of the θ profile; see (9).

The functional form chosen for $M(y)$, called the 'triplet map,' is the simplest of a class of mappings that satisfy the physical requirements of measure preservation (the nonlocal analog of vanishing velocity divergence), property continuity (no introduction of property-profile discontinuities by the mapping operation), and scale locality (at most order-unity changes in property gradients). The first two requirements are fundamental properties of advection. The requirement of scale locality is based on the well-established principle that length-scale reduction in a turbulent cascade occurs by a sequence of small steps (corresponding to turbulent eddies), causing down-scale transfer of energy and of property fluctuations to be effectively local in wavenumber.

Mathematically, the triplet map is defined as

$$M(z) \equiv z_0 + \begin{cases} 3(z-z_0) & \text{if } z_0 \le z \le z_0 + \frac{1}{3}l, \\ 2l - 3(z-z_0) & \text{if } z_0 + \frac{1}{3}l \le z \le z_0 + \frac{2}{3}l, \\ 3(z-z_0) - 2l & \text{if } z_0 + \frac{2}{3}l \le z \le z_0 + l, \\ z - z_0 & \text{otherwise.} \end{cases} \quad (6)$$

This mapping takes a line segment $[z_0, z_0 + l]$, shrinks it to a third of its original length, and then places three copies on the original domain. The middle copy is reversed, which maintains the continuity of advected fields and introduces the rotational folding effect of turbulent eddy motion. Property fields outside the size-l segment are unaffected.

The discrete numerical representation of the triplet map is described and illustrated in Sec. 2.2. There, the integer quantities Z and $3S$ are the discrete analogs of the parameters z_0 and l, respectively.

In (5), K is a kernel function that is defined as $K(z) = z - M(z)$, i.e., its value is equal to the distance the local fluid element is displaced. It is non-zero only within the eddy interval, and it integrates to zero so that the process does not change the total (z-integrated) momentum of individual velocity components. It provides a mechanism for energy redistribution among velocity components, enabling the model to simulate the tendency of turbulent eddies to drive the flow toward isotropy, constrained by the requirement of total (kinetic plus potential) energy conservation during the eddy event (which is non-dissipative).

To quantify these features of eddy energetics,

and thereby specify the coefficients c_s in (5), it is convenient to introduce the quantities

$$s_K \equiv \frac{1}{l^2}\int s(M(z))K(z)\,dz, \tag{7}$$

where $s = u$, v, w, or θ. Substitution of the definition of $K(z)$ into (7) yields the equivalent expression

$$s_K \equiv \frac{1}{l^2}\int [s(M(z)) - s(z)]z\,dz. \tag{8}$$

For $s = \theta$, this expression is proportional to the potential-energy change induced by the triplet map. The energy change Δ caused by an eddy event can then be expressed as

$$\begin{aligned}\Delta = \quad & \rho_0 l^2 (c_u u_K + c_v v_k + c_w w_K) \\ & + \tfrac{2}{27}\rho_0 l^3 (c_u^2 + c_v^2 + c_w^2) - \rho_0 g l^2 \tfrac{\theta_K}{T_0}.\end{aligned} \tag{9}$$

Here, the Boussinesq approximation is adopted, and accordingly a reference density ρ_0 (defined here as mass per unit height, based on a nominal column cross-section) and a reference potential temperature T_0 are introduced, as well as the gravitational acceleration g.

The representation of both the potential and kinetic energy contributions in (9) using (7) is a consequence of the definition chosen for K. Based on this definition, another equivalent form of (7),

$$s_K \equiv \frac{4}{9l^2}\int_{z_0}^{z_0+l} s(z)[l - 2(z - z_0)]\,dz, \tag{10}$$

which is useful for numerical implementation, is readily obtained.

Overall energy conservation requires $\Delta = 0$. Two additional conditions are required to specify the coefficients c_s. These are based on a representation of the tendency for eddies to induce isotropy. For this purpose, it is noted that there is a maximum amount $Q_s = \frac{27}{8}\rho_0 l s_K^2$ of kinetic energy that can be extracted from a given velocity component during an eddy event (Kerstein et al., 2001). (The amount of energy extracted or deposited depends on c_s.) Q_s is thus the 'available energy' in component s prior to event implementation. The tendency toward isotropy is introduced by requiring the available energies of the three velocity components to be equal upon completion of the eddy event. This provides the additional needed conditions and yields the following expression determining c_s:

$$c_s = \frac{27}{4l}\left[-s_K \pm \sqrt{\frac{1}{3}\left(u_K^2 + v_K^2 + w_K^2 + \frac{8gl}{27}\frac{\theta_K}{T_0}\right)}\right]. \tag{11}$$

The physical criterion that resolves the sign ambiguity is explained by Kerstein et al. (2001). Note that the last term in (11) is the square root of a quantity proportional to the net available energy $Q_u + Q_v + Q_w - P$, where the quantities Q_s are the component available energies prior to event implementation and P is the gravitational potential energy change caused by triplet-mapping of the θ profile, requiring equal-and-opposite change of available energy during eddy implementation, as enforced by the condition $\Delta = 0$. If P is positive (stable stratification) and larger than the available energy, then the eddy is energetically prohibited. In this case, the argument of the square root in (11) is negative and the eddy event is not implemented (see Sec. 3.4).

3.4 Eddy Selection

Although the formulation of an individual eddy event incorporates several important features of turbulent eddies, the key to the overall performance of the model is the procedure for determining the sequence of eddy events during a simulated flow realization. It is assumed that the expected number of eddies occurring during a time interval dt, whose parameter values are within dz of z_0 and within dl of l, is $\lambda(z_0, l; t)\,dz_0\,dl\,dt$, where the 'eddy rate distribution' λ has units of (length$^2\times$time)$^{-1}$. Eddies are randomly sampled from this distribution. Mathematically, this generates a marked Poisson process whose mean rate as a function of the 'mark' (parameter) values z_0 and l varies with time. The physical content of the eddy selection process is embodied in the expression for λ that is adopted:

$$\lambda = \frac{C\nu}{l^4}\sqrt{R_u^2 + R_v^2 + R_w^2 + \frac{8gl^3}{27\nu^2}\frac{\theta_K}{T_0} - Z}, \tag{12}$$

where $R_s \equiv s_K l/\nu$. This expression involves two free parameters, C and Z, whose roles in the present context are explained in Sec. 3.5. λ is set equal to zero if the argument of the square root is negative, indicating an energetically prohibited event; see the discussion of (11).

For $Z = 0$, the argument of the square root is a scaled form of the net available energy. Thus, for

given z_0 and l, (12) with $Z = 0$ is simply the dimensionally consistent relation between the net available energy and the length and time scales of eddy motion, where the associated time scale is the inverse of the (appropriately normalized) eddy rate λ.

For example, assume $Z = 0$ and assume that all properties except u are constant in a given z range. In this range, assume that $u = \sigma z$, where σ is the only non-zero strain component within the z range. For any eddy within this range, $1/\sigma$ is the mixing-length scaling estimate of the turnover time. From (10), u_K is of order σl for a size-l eddy. (12) then gives $\lambda \sim \sigma/l^2$. In ODT, the inverse of the corresponding turnover time of an eddy of given nominal size l_1 is estimated by integrating $\lambda(z_0, l)$ over a corresponding geometric l interval (e.g. $[l_1, 2l_1]$) and z_0 interval (e.g., $[0, l_1]$). For the case under consideration, an inverse turnover time of order σ is obtained, consistent with mixing-length scaling.

Suppose instead that the only non-constant property is θ, and that $\theta/T_0 = \sigma z$, where σ is now an inverse length. Then both mixing-length estimation and the analogous derivation based on (12) yield the turnover-time estimate $(g\sigma)^{-1/2}$.

Application of similar reasoning to near-wall turbulent flow likewise indicates the consistency of (12) with mixing-length phenomenology, in this case with an explicitly identified mixing length (distance from the wall), reflecting flow inhomogeneity. The mixing-length analysis is more elaborate in this instance, and is not presented here, but demonstrations of model consistency with the phenomenology of turbulent boundary layers are provided in Sec. 4.1.

Thus, (12) may be viewed as a representation of mixing-length phenomenology within the ODT framework. This representation differs fundamentally from the typical use of mixing-length concepts to close averaged equations in several respects:

1. Rather than assigning a unique l value at each spatial location, ODT allows eddies of all sizes throughout the spatial domain, with their relative frequencies of occurrence at different locations specified by (12).

2. Quantities on the right-hand side of (12) depend on the instantaneous flow state rather than an average state, so eddy occurrences are responsive to unsteadiness resulting from transient forcing or statistical fluctuations inherent in the eddy-sampling process.

3. Eddy occurrences thus depend on prior eddy events and affect future eddy occurrences. These dependencies induce spatiotemporal correlations among eddy events, leading to a physically based representation of turbulence intermittency.

These attributes of ODT are the basis of its detailed representation of turbulent cascade dynamics coupled to boundary conditions, shear and buoyant forcing, etc. In particular, the stochastic variability of simulated ODT realizations arises from a physically based representation of turbulent eddy statistics, and thus enables a conceptually sound and mathematically consistent assessment of the effects of stochastic variability on the variability of, and correlations among, output statistics.

The unsteadiness of the rate distribution λ suggests the need to continuously reconstruct this distribution as the flow state evolves. This prohibitively costly procedure is avoided by an application of the rejection method, which involves eddy sampling based on an arbitrary time-invariant rate distribution that is designed to over-sample all eddies. True rates are computed only for sampled eddies, and are used to determine eddy rejection probabilities. The resulting procedure adequately approximates the desired sampling from λ (Kerstein, 1999); it is exact in the limit of infinite over-sampling.

If two of the three velocity components are removed from the model, (12) reduces to the eddy rate distribution used by Wunsch and Kerstein (2001). If the buoyancy term is omitted, (12) resembles the expression for λ that appears in Kerstein et al. (2001), except that here, λ is based on the total available energy (including contributions from all three velocity components) rather than the available energy associated with vertical motion. Use of the total available energy is advantageous here because it gives the correct critical Richardson number, $Ri_c = \frac{1}{4}$, for the onset of instability (in the present context, eddy events). Another distinction from Kerstein et al. (2001) is that the procedure that was used previously to suppress occasional unphysically large eddy events is omitted here. For the present application, the stable stratification suffices to prevent such anomalies.

3.5 Constant-Viscosity Formulation

Because molecular-transport processes are negligible away from the near-surface region, it is unnecessary (and unaffordable, even in 1D) to resolve them throughout the vertical extent of the ABL. In fact, they need not be resolved near the surface either, because there they are dominated by roughness effects. Therefore the viscosity ν is treated as an adjustable parameter, assigned a fixed value that provides an empirical representation of surface roughness.

The assignment is based on the near-surface boundary-layer structure that is resolved by ODT. If ν is taken to be the molecular viscosity, then the ODT simulation is a fully resolved representation of the dynamics of the flow near a smooth surface. If this representation is accurate, then the ODT mean velocity profile should capture the viscous, buffer, and log layers respectively. ODT simulations of Couette and channel flow (Kerstein, 1999; Schmidt et al., 2003) do in fact reproduce this structure, and quantitatively accurate results are obtained by adjustment of the parameters C and Z.

The empirical representation of roughness is based on the respective roles of C and Z in (12). Z determines a threshold Reynolds number for eddy turnover. (If the quantity under the square root is negative, the eddy event is disallowed.) In a boundary layer, Z controls the viscous suppression of near-wall eddies, and thus the extent of the buffer layer. C scales the overall event rate and thus the turbulence intensity. Therefore the choice of C directly affects turbulent transport in the log layer, and indirectly affects the viscous and buffer layers through the interactions among layers. The net effect is that the von Karman constant κ increases with increasing C.

In this application, roughness is modeled as a viscosity enhancement, so ν is an effective viscosity representing roughness effects rather than the molecular viscosity. Specifically, the viscosity is adjusted so that the mean velocity $m = (\langle u\rangle^2 + \langle v\rangle^2)^{1/2}$ obeys viscous scaling, $m/u_* = z/z_*$, from $z = 0$ to the roughness height z_0, where $z_* = \nu/u_*$. (Note that z_0 has a different meaning here than earlier.) Based on this picture, the friction velocity, which is conventionally defined as $u_* = \left(\langle u'w'\rangle_s^2 + \langle v'w'\rangle_s^2\right)^{1/4}$ (where s denotes a surface value) is instead expressed as

$$u_* = \nu^{1/2}\left[\langle \partial_z u\rangle_s^2 + \langle \partial_z v\rangle_s^2\right]^{1/4}. \qquad (13)$$

Implementation of this procedure for the intercomparison case is discussed in Sec. 4.1.1. For the value $z_0 = 0.1$ m used in the intercomparison, this height exceeds the extent of the buffer layer that would appear in the boundary layer above a flat surface, so it is assumed that buffer-layer effects are subsumed within the roughness-dominated region. For this reason, Z is set equal to zero. For Couette flow with $Z = 0$, ODT mean velocity profiles transition from viscous to log scaling over a short z_* interval, with no inflection point (in semilog coordinates). Log scaling with $\kappa = 0.4$ is obtained for $C = 9.3$. Accordingly, the parameter values $Z = 0$, $C = 9.3$ are used for ODT simulation of the intercomparison case.

The Prandtl number of air is 0.7. Turbulent heat transfer studies indicate that this is also a reasonable value for the turbulent Prandtl number, so γ in (4) is assigned the value $\nu/0.7$. Note that the turbulent Prandtl number is used here to specify subgrid heat transport, but mesh-resolved heat transport is governed by model dynamics (eddy events) rather than an assigned turbulent Prandtl number.

The initial and boundary conditions of the ODT simulation are as specified for the intercomparison, except that the initial u profile has a linear ramp from $z = 0$ to $z = 4$ m to avoid possible numerical problems resulting from extremely high local shear near $z = 0$. Above $z = 4$ m, $u = U_g = 8$ m/s initially. Initially, $v = V_g = 0$ m/s, $w = 0$ m/s, and $\theta = \theta_0 = 265$ K from the surface to $z = 100$ m, then increasing at 0.01 K/m to the domain top ($H = 400$ m), where $\theta = \theta_0 + \Delta\theta = 268$ K initially. The specified surface cooling rate is $\dot{\theta}_g = 0.25$ K/h. Reference constants are $g = 9.81$ m/s^2, $f = 0.000139$ s^{-1}, $T_0 = 263.5$ K, and $\rho_0 = 1.3223$ kg/m^2.

3.6 Variable-Viscosity Formulation

An ODT formulation that is more closely analogous to LES than the constant-viscosity formulation is obtained by introducing an eddy viscosity based on a local estimate of the transport associated with all eddy events up to the smallest resolved event. In the discrete numerical implementation of eddy events, the smallest resolved event spans six grid cells (Kerstein, 1991).

For this purpose, a local approximation of the eddy rate distribution is obtained by assuming linear dependence on z of the variable s in the integrand of (10), giving $s_K = -\frac{2}{27} D_s l$, where D_s is the slope of the s profile at the location where the eddy viscosity is being evaluated. Substitution of this approximation into (12), with $Z = 0$ as explained earlier, gives

$$\lambda = \frac{2}{27 l^2} \sqrt{D_u^2 + D_v^2 + D_w^2 - \frac{27}{2} g D_\theta}. \qquad (14)$$

This approximate form is adopted for eddy-viscosity computation because this computation is performed at every diffusion time step in every mesh cell, so it is desirable to minimize the computational cost. Results are not very sensitive to details of the eddy-viscosity profile, so the approximate computation is adequate for this purpose.

Using (14), the dimensionless eddy viscosity ν' is expressed as

$$\nu = \frac{1}{2} B \int_0^{\hat{l}} \langle \delta^2 \rangle \lambda l \, dl = \frac{2}{27} B I \int_0^{\hat{l}} \lambda l^3 \, dl, \qquad (15)$$

where $\langle \delta^2 \rangle = \frac{4}{27} I l^2$ is the mean-square displacement of fluid within a size-l eddy by a triplet map and ν is evaluated by integrating over all eddies smaller than the marginally resolved eddy (whose size is denoted $\hat{l}$) that contain the location at which ν is being evaluated. The factor $\frac{1}{2}$ in front of the first integral is from the relation between the transport coefficient and underlying rate distribution of random displacements. The factor I in the expression for the mapping-induced mean-square displacement is a correction of the continuum result that accounts for the spatially discrete implementation of the triplet map. For a six-cell eddy, which is the smallest resolved eddy in the current numerical implementation, $I = \frac{1}{2}$. The factor B is a free parameter. Here, it is adjusted to match the constant-viscosity ODT results; see Sec. 4.

Substitution of (14) into (15) gives

$$\nu = \frac{2}{729} B I \hat{l}^2 \sqrt{D_u^2 + D_v^2 + D_w^2 - \frac{27}{2} g D_\theta}. \qquad (16)$$

A modification of this result is applied near the surface. At a given location far from the surface, six different six-cell eddies can contain a given cell. Near the surface however, j different six-cell eddies can contain cell j for $j < 6$. This reduces the transport induced by six-cell eddies for $j < 6$. Adopting the simple but imprecise assumption that the induced transport is independent of cell location within the eddy, this near-surface effect is incorporated by multiplying the right-hand side of (16) by $\min(j, 6)$, where j is the cell index referenced to the surface (which is nominally at $j = 0$).

In numerical implementation, ν is assigned a lower bound corresponding to a small fraction of its value adjacent to the surface. For this purpose, the surface value is computed with the gravitational term omitted to avoid a negative value in the square root. The lower bound supercedes the result given by (16) whenever the argument of the square root is either very small or negative. Tests indicate negligible sensitivity to the chosen fraction. As in the constant-viscosity formulation, the thermal diffusivity is determined from the viscosity by assuming $Pr = 0.7$, where as earlier, Pr is a subgrid turbulent Prandtl number in this context.

The model parameter C, as well as B, is adjusted in the variable-viscosity implementation because this is found to be necessary in order to obtain reasonable conformance to the constant-viscosity results. The adjustment of B has some theoretical justification due to the approximate nature of the closure assumptions. The adjustment of C has less justification because one would not expect the quantitative relation between large-scale forcing (shear, gravitation) and turbulence production to depend on the subgrid closure. The need for this adjustment possibly reflects the role of near-surface fine-scale dynamics that influence the fluxes of heat and momentum to the surface. The adjustment of C may be needed to compensate for the lack of resolution of the fine-scale processes that control these fluxes, which in turn control bulk-flow structure and development.

The initial conditions and additional parameters used to simulate the intercomparison case with this formulation are the same as those given in Sec. 3.5 for the constant-viscosity formulation, except that the initial ramp portion of the u profile extends to 20 m instead of 4 m.

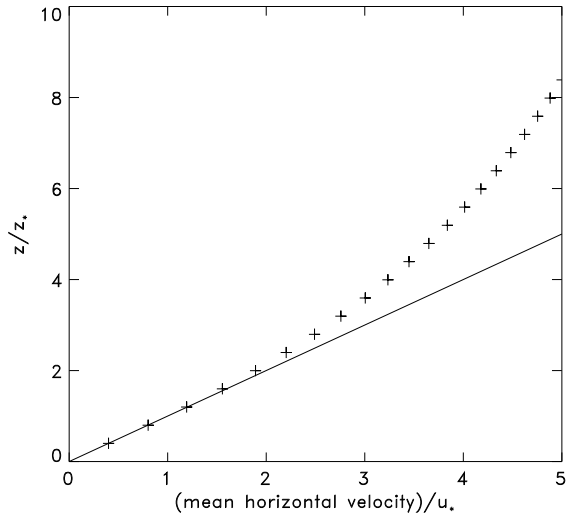

Figure 2: Near-surface mean horizontal velocity based on the final hour of simulation (+), compared to viscous scaling (solid).

4 RESULTS

4.1 Constant-Viscosity Formulation

4.1.1 Viscosity Adjustment

As explained in Sec. 3.5, the viscosity used in ODT simulation of the intercomparison case is chosen so that the mean horizontal velocity obeys viscous scaling, $m/u_* = z/z_*$, for $z \leq z_0$, where $z_0 = 0.1$ m is the roughness height for the intercomparison case. For the ODT parameter values $C = 9.3$ and $Z = 0$ used to simulate this case (see Sec. 3.5), this condition is satisfied for $\nu = 0.02$ m^2/s, which is therefore the viscosity value used for this application.

Figure 2 shows a portion of the wall-scaled mean velocity profile based on the last hour of simulation (hour 9, the averaging period for all averaged vertical profiles shown here). Plotted constant-viscosity results are based on one simulated realization, except where it is indicated that an average of ten simulated realizations was used to reduce variability. To resolve the viscous layer well enough so that the numerical simulation closely approximates the continuum limit, a mesh spacing of 0.025 m is used, requiring 16000 mesh points to span the 400 m domain height. For larger ν, a coarser mesh would provide adequate resolution. In the present context, variation of ν would provide an indication of roughness-height sensitivity.

The plot demonstrates viscous scaling up to four mesh spacings above the surface, corresponding to the target value $z_0 = 0.1$ m. The plot also indicates that the simulation resolves $z/z_* = 0.4$.

The choice $\nu = 0.02$ m^2/s has little apparent effect on simulated ABL evolution beyond the viscous layer, other than its essential role as the mechanism of kinetic-energy dissipation. For this ν value, velocity fluctuations are adequately resolved on the 16000-cell mesh. Thus, $\nu = 0.02$ m^2/s is sufficiently dissipative without contributing significantly to total transport (except in the near-surface region).

To assess the effect of running the simulation with larger ν on a coarser mesh, a case was run with $\nu = 1$ m^2/s on a 200-cell mesh. The ABL grew much too rapidly. For ν this large, viscous momentum transfer (in effect, eddy viscosity) dominates transport by ODT eddy events. ODT simulation on a mesh this coarse requires a more sophisticated determination of ν than simply assigning a constant value. This is the motivation for introducing the variable-viscosity formulation (Sec. 3.6).

4.1.2 Mean Profiles

Figure 3 shows the mean horizontal velocity plotted in wall coordinates. A line segment corresponding to log scaling with $\kappa = 0.4$ is shown for comparison. The short duration of the simulation and effects of transient evolution may cause the log scaling to be less precise than for simulations of statistically steady confined flows. Nevertheless, consistency with $\kappa = 0.4$ is apparent.

Figure 4 shows the vertical profile of the mean u velocity. The velocity at the surface appears to be greater than zero because the near-surface high-gradient region is not discernible in this format. Models lacking the spatial resolution and/or physical mechanisms required to simulate the near-surface flow may not capture large near-surface increments of velocity and other properties.

The normalized Ekman spiral based on the mean velocities is shown in Figure 5 and the mean potential temperature is shown in Figure 6. These profiles are consistent with the LES results of Kosovic and Curry (2000) as well as LES results reported in the GABLS intercomparison.

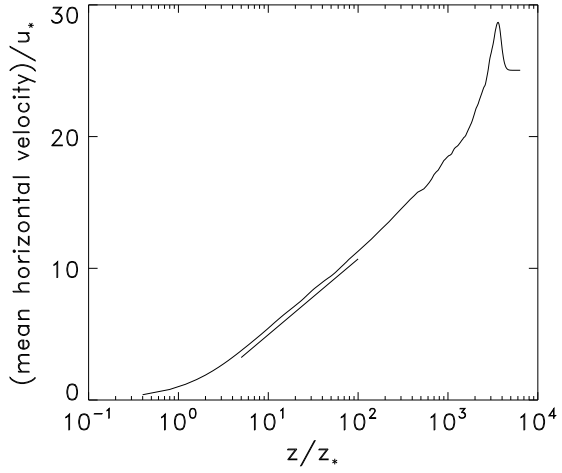

Figure 3: Mean horizontal velocity in wall coordinates (curve), compared to log scaling with $\kappa = 0.4$ (line segment).

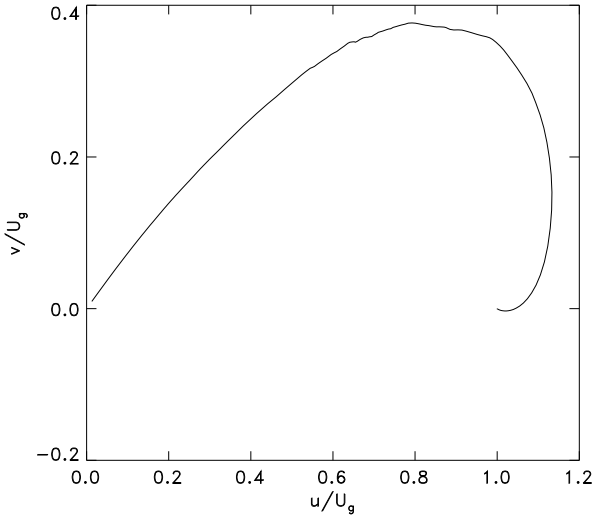

Figure 5: Normalized Ekman spiral.

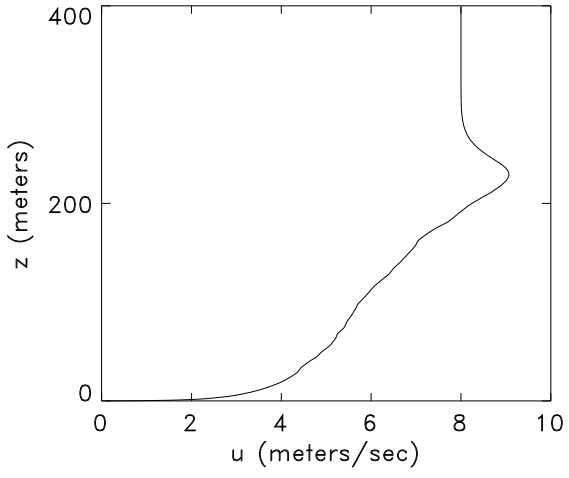

Figure 4: Vertical profile of mean u velocity.

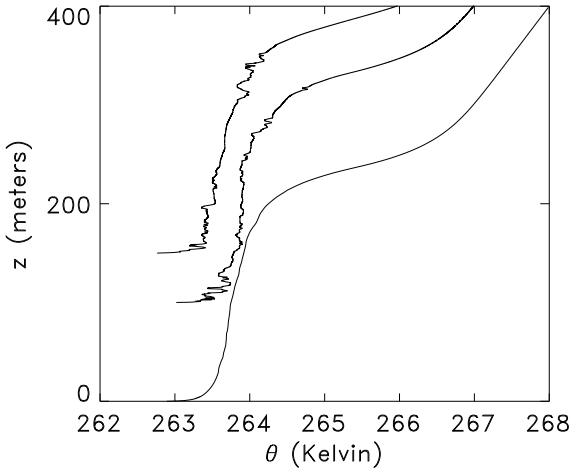

Figure 6: Vertical profiles of mean potential temperature and of instantaneous potential temperature at the beginning and end of the averaging period (displaced upward 100 m and 150 m, respectively).

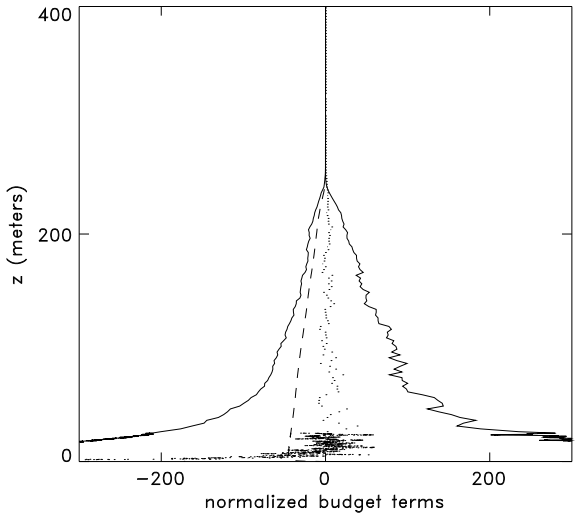

Figure 7: TKE budget terms scaled by $u_*^2 f$: production (solid; positive), dissipation (solid; negative), buoyant production (dash), total transport (points). Results are based on ten simulated realizations.

Instantaneous profiles are are also shown in Figure 6 to illustrate structural variability during the simulations and to highlight the large near-surface gradients.

4.1.3 Fluctuation Profiles

Vertical profiles of selected fluctuation statistics are shown in plots in Sec. 4.2 that compare results for the two viscosity closure methods. Despite the vertical binning over most of the domain (see Sec. 4.1.2), the profiles are noisy. This reflects the fact that the ODT is an unsteady simulation capturing individual eddy motions, like LES, but is 1D and therefore involves no horizontal averaging, like other SCMs. Despite the variability, the gross features are reproducible, as indicated by comparisons (not shown here) to results for the previous averaging period and to a run using a different random number seed.

The total transport in the plot of TKE budget terms in Figure 7 is noise-dominated. The noise was reduced by averaging over ten simulated realizations. It appears that averaging over a larger number of realizations would further reduce the noise, giving a small transport contribution compared to the dominant budget terms, as in LES (Kosovic and Curry, 2000).

Near the surface, fluctuation properties are similar to results previously reported for channel flow (Schmidt et al., 2003), with minor differences due to the differences in parameter values and in some details of the model formulation (Sec. 3). In particular, total transport is non-negligible near the surface but it is adequately resolved there. (One hour is sufficient averaging time for near-surface statistics because the time scale of the dominant near-surface eddies is shorter than the dominant time scale away from the surface.) The production and dissipation profiles attain much larger values (off scale in Figure 7) near the surface than in LES (Kosovic and Curry, 2000) because they transition in ODT from dependence on bulk parameters (u_* and f) to dependence on wall parameters (u_* and ν). For a smooth surface, the near-surface structure predicted by fully resolved ODT is physically realistic, as indicated by previous comparisons (Schmidt et al., 2003) to direct-numerical-simulation results.

4.2 Variable-Viscosity Formulation

The formulation of Sec. 3.6 was applied to the GABLS setup for two different meshes, each uniform, partitioning the 400 m vertical domain into 64 and 128 cells, respectively. For both cases, C was set equal to unity. B was set equal to 15 and 40 for the respective cases. The need for larger B at the higher resolution may be due to the inability of the coarse-grained computation to generate realistically high property gradients at the surface. Therefore as the resolution increases, resulting in lower transport coefficients based on the closure formulation, B must be increased to maintain the magnitude of the surface fluxes.

The underlying problem is that the transport coefficients have two different, not necessarily compatible roles. One is to provide the correct dissipation of marginally resolved property fluctuations, which in reality are dissipated by turbulent cascading to smaller scales. The other is to transport these properties correctly where the mesh-resolved advection is not the dominant transport mechanism (e.g., near the surface). These are two different physical processes obeying different scalings that are not readily accommodated in a closure as simple as the approach used here. A more elaborate closure, such as the method involving an evolution equation

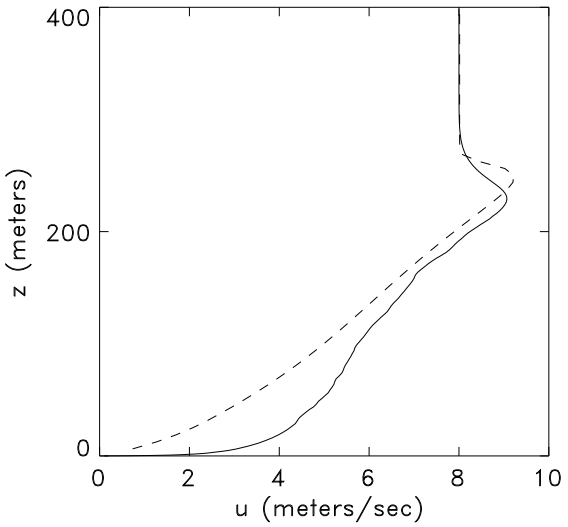

Figure 8: Vertical profiles of mean u velocity for cases H (solid) and L (dash).

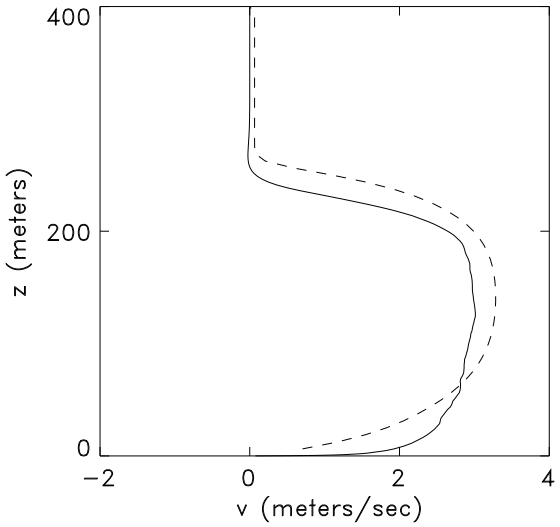

Figure 9: Vertical profiles of mean v velocity for cases H (solid) and L (dash).

for subgrid-scale turbulent kinetic energy that is used by Kosovic and Curry (2000), following Moeng (1984), might be more suitable in this regard. The simpler method is used here in order to maintain focus on ODT performance, unencumbered by a subgrid treatment that would introduce additional complexity and empiricism. It is possible that this method will be adequate for simulations with prescribed surface fluxes, which is a suitable surface coupling for many situations.

Due to their low cost, the low-resolution cases were run for 10,000 realizations each in order to obtain ensemble-averaged results. (The 64-cell case runs in 3 seconds, compared to a two-day run time for the 16000-cell constant-viscosity computation.) This compensates for the absence of horizontal coordinates over which to average the results. The individual realizations at low resolution are at least as variable as the constant-viscosity realization, but this is not reflected in the plotted comparisons due to the ensemble averaging of the low-resolution cases. (Some of the plotted high-resolution results are averages over ten simulated realizations.)

Representative flow statistics are shown in Figures 8-21. Results for the 64-cell and 128-cell meshes are consistently very close to each other, so the 128-cell results are not shown. Except for time series, all quantities are averaged over the last hour of the simulation, as in Sec. 4.1. Here, simulations involving 16000 and 64 cells are denoted cases H (high resolution) and L (low resolution), respectively. Richardson-number profiles for a single realization are very noisy, so case-H results averaged over ten simulated realizations are shown in figure 11. (In all instances, case-H results for a single realization and for multiple realizations are the same except for the reduction of variability due to averaging over multiple realizations. This does not hold, however, for case-L results, as noted shortly.) The case-L Ri profiles are fairly close to those of Kosovic and Curry (2000), but the case-H Ri values are somewhat higher.

Time histories for case H, plotted as points at one-minute intervals, are likewise very noisy. Accordingly, the case-H histories shown in figures 12-14 averages over ten simulated realizations. The results are consistent with those for case L, which are smooth curves due to averaging over a much larger ensemble.

Based on the adjustment of two free parameters, the case-L methodology is found to give a reasonable representation of various mean properties and fluxes, but fluctuation statistics exhibit substantial artifacts. Case-H variance profiles generally agree with LES results of Kosovic and Curry (2000) with regard to profile shapes and relative magnitudes of component

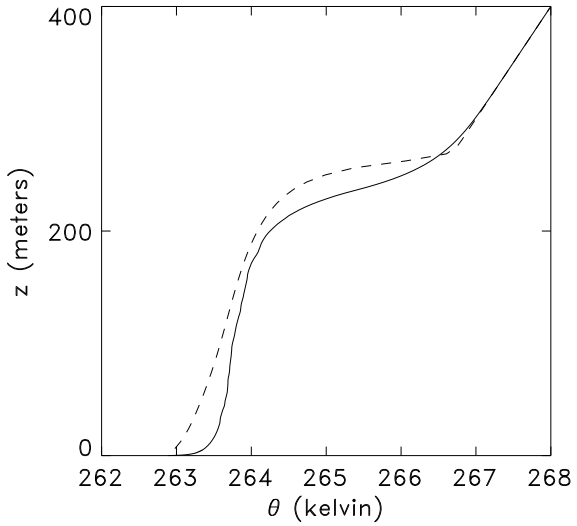

Figure 10: Vertical profiles of mean potential temperature for cases H (solid) and L (dash).

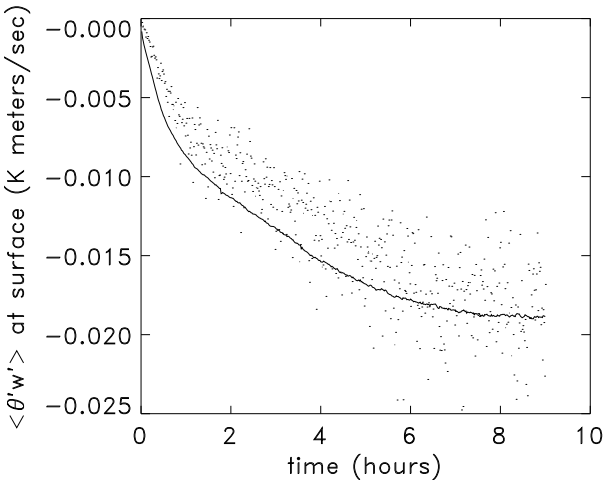

Figure 12: Time history of surface potential temperature flux for cases H (dot), based on ten realizations, and L (solid).

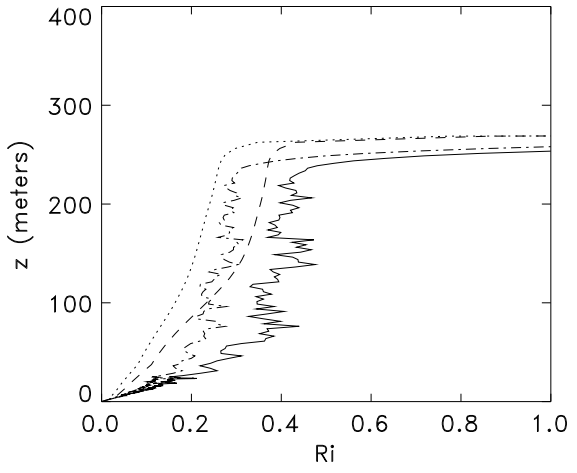

Figure 11: Vertical profiles of mean Richardson numbers (flux, gradient) for cases H (solid, dot-dash), based on ten realizations, and L (dash, dot).

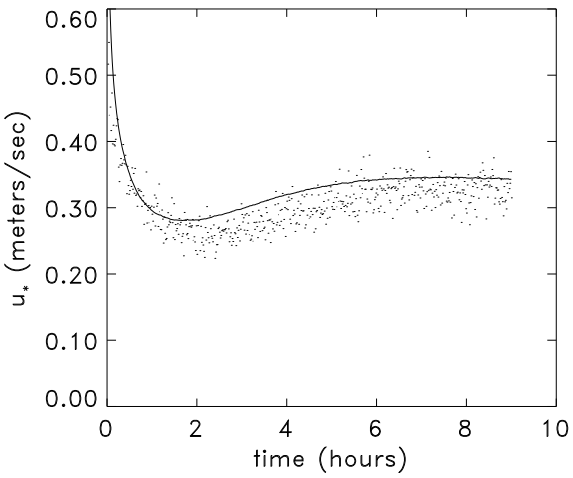

Figure 13: Time history of friction velocity for cases H (dot), based on ten realizations, and L (solid).

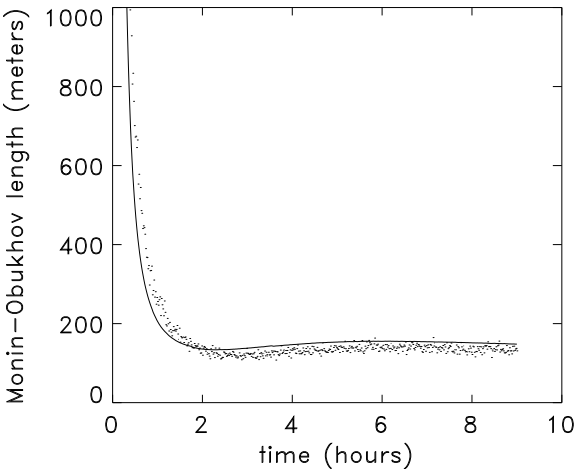

Figure 14: Time history of Monin-Obukhov length for cases H (dot), based on ten realizations, and L (solid).

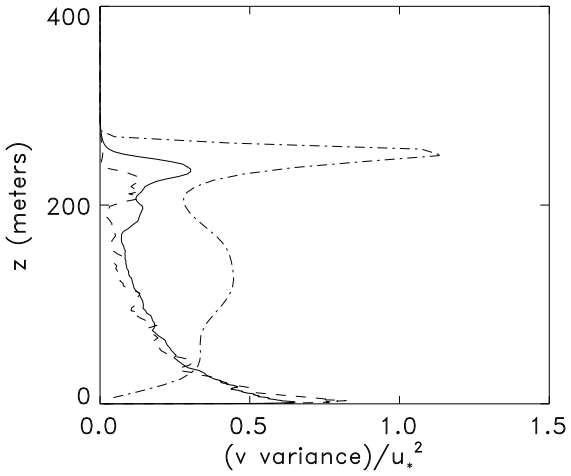

Figure 16: Vertical profiles of scaled v variance for for case L (dot-dash) and for case H based on one realization (dash) and an ensemble of ten realizations (solid).

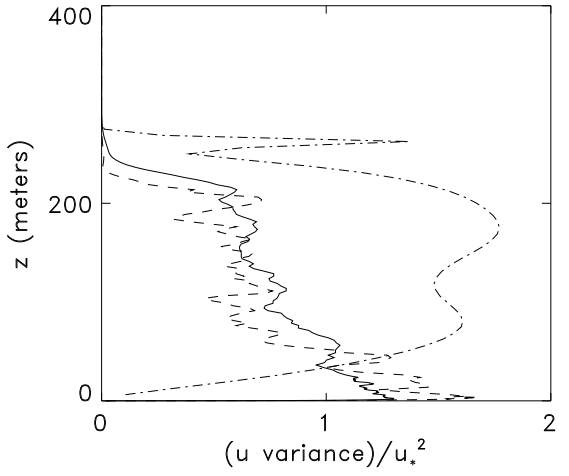

Figure 15: Vertical profiles of scaled u variance for for case L (dot-dash) and for case H based on one realization (dash) and an ensemble of ten realizations (solid).

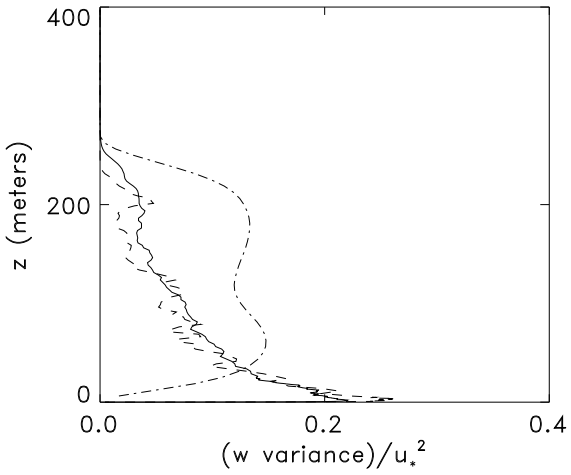

Figure 17: Vertical profiles of scaled w variance for for case L (dot-dash) and for case H based on one realization (dash) and an ensemble of ten realizations (solid).

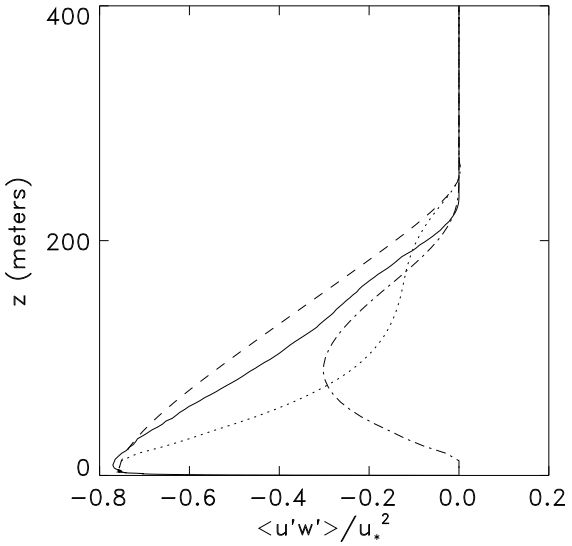

Figure 18: Vertical profiles of scaled u flux for case H (solid) and case L: total (dash), resolved (dot-dash), subgrid (dot).

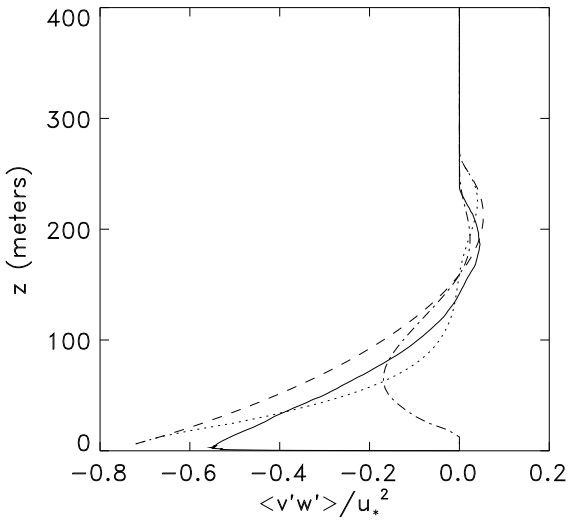

Figure 19: Vertical profiles of scaled v flux, for case H (solid) and case L: total (dash), resolved (dot-dash), subgrid (dot).

variances, but are low relative to the LES profiles. The profiles for one and for multiple realizations are similar in character, indicating that the differences among realizations are no greater than the variability within a realization. In contrast, it is found that variance profiles for single realizations of case L (not shown), though very erratic, are lower in overall magnitude than the ensemble-averaged profiles of figures 15-17. This indicates that differences among realizations are the main source of variability. A further indication is that the sharp peaks of the case-L u and v variance profiles at the top of the mixed region are not seen in variance profiles for single realizations. Because eddy transport is largely suppressed at this location (e.g., figure 18), these peaks do not reflect variability within a simulated realization. Rather, they reflect the variability of the depth of the mixed region from realization to realization. This is a fundamentally different source of variability than for case H, or for LES of this flow, and may account for the evident artifacts.

Case L may have higher intrinsic variability because the parameter C controlling the overall rate of eddy events has been reduced by almost an order of magnitude relative to case H, thereby reducing the number of large transport-controlling eddy events per realization. (Domain coarsening greatly reduces the total number of eddies, but eddies eliminated in this manner are generally too small to have much effect on fluctuation statistics.)

Figures 18-20 indicate that case-L flux profiles agree fairly well with those for case H. The also are consistent with LES results (Kosovic and Curry, 2000). It is useful to compare figure 20 to the plot of total and subgrid potential temperature flux in that LES study. Qualitatively, the case-L subgrid contribution resembles the LES subgrid profile in that it dominates the resolved contribution near the surface and at the top of the mixed region and levels off in between. Quantitatively, there are important differences that reflect limitations of the case-L methodology. In particular, the near-surface subgrid dominance is confined to the a tenth of the mixed-region depth in the LES but subsumes almost half of the mixed region for case L.

This quantitative difference is reflected in the case-L TKE budget, shown in figure 21. As in the LES (Kosovic and Curry, 2000), budget terms decrease in magnitude in the region of near-surface subgrid dominance. This effect is seen only in the lowest five percent of the mixed region in the LES, but in figure 21 it is seen in the lower half of the mixed region. In the upper half, the behavior is in reasonable conformance with LES

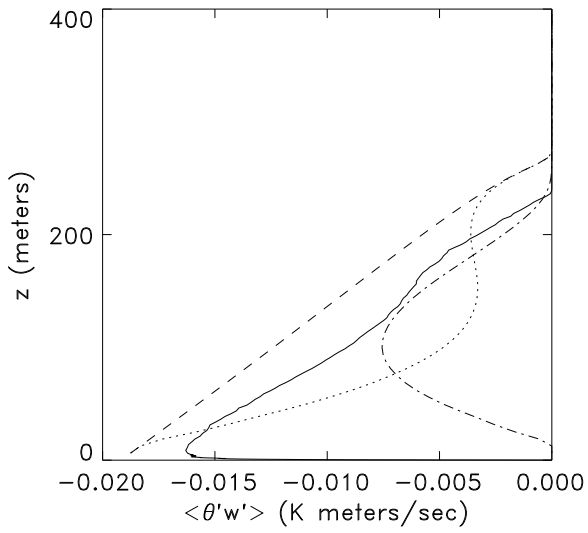

Figure 20: Vertical profiles of potential temperature flux, for case H (solid) and case L: total (dash), resolved (dot-dash), subgrid (dot).

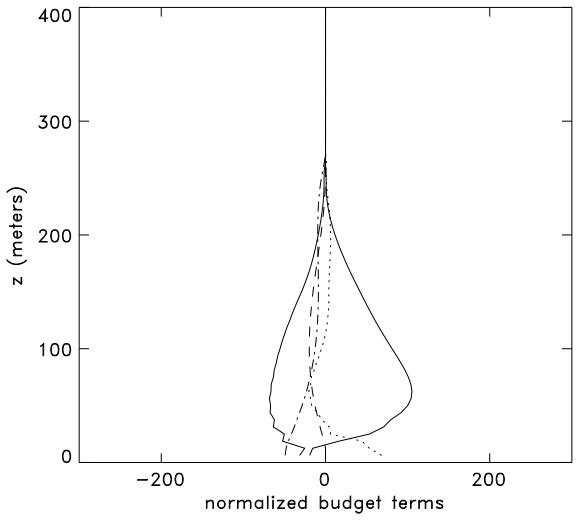

Figure 21: For case L, TKE budget terms scaled by $u_*^2 f$ (resolved quantities except where indicated): production (solid; positive), dissipation (solid; negative), buoyant production (dash), total transport (dot), subgrid buoyant production (dot-dash).

results. In contrast, case-H results (figure 7) resolve budget profiles much closer to the surface than the LES can capture.

Figure 21 illustrates another artifact of the case-L methodology. As formulated, it yields balance of the resolved budget terms. However, for case L, there is a substantial subgrid buoyant production that introduces an imbalance if not compensated by other subgrid terms. The present closure dissipates all energy removed from the grid and therefore cannot reconcile this imbalance. The case-H TKE budget is subject to the same artifact, but its quantitative impact is much smaller because the mesh resolves nearly all advective motion in that simulation.

Introduction of a subgrid TKE evolution equation and associated phenomenology, as in Kosovic and Curry (2000), would provide complete balance and thus remove the artifact. This would have the additional advantage of enforcing greater consistency, and thus comparability, of ODT and LES results.

5 DISCUSSION

Various 1D methodologies provide reasonable representations of the stably stratified ABL, as indicated by the GABLS intercomparison study. A unique attribute of ODT in this regard, when implemented using the constant-viscosity subgrid closure method, is its prediction of the intercomparison case with no tuning of parameters to match LES results or other data for this flow. Adopting a straightforward phenomenological representation of roughness effects, the only required empirical inputs other than the case specification are the von Karman constant and the turbulent Prandtl number. Like any 1D approach, this formulation is economical compared to LES, but within the 1D context it is costly, requiring 16000 mesh cells spanning the 400 m domain, with commensurate time-step constraints.

The computational cost can be reduced to that of conventional SCMs by introducing a more empirical subgrid closure. Here, a purely dissipative closure that is minimal in complexity, within the ODT framework, has been introduced. Although ODT with this variable-viscosity closure can be viewed as an LES surrogate in some respects, the results obtained for LES-like vertical resolution do not indicate LES-like performance. It is shown that limitations of the closure are the likely explanation. In future work, a closure

more directly analogous to LES closure methodology, involving more empiricism but capturing more of the relevant subgrid physics, will be implemented in ODT. The ultimate goal is to obtain a cost-effective tool for simulation of vertical transport and mixing for ABL conditions that can be adequately treated within a single-column framework. To realize its potential in this regard, the phenomenology usually included in SCMs (radiation, moist processes, etc.) will be incorporated into ODT.

With these additions, the model setup introduced here will be applied to other cases that are dominated by vertical transport and entrainment, such as the DYCOMS intercomparison (Stevens, 2003). The demonstrated capability of ODT to capture buoyancy-reversal effects (Wunsch, 2003) is pertinent in this regard.

ODT has also been applied to buoyant stratified flow using a horizontal 1D domain, thereby capturing horizontal shear generated by the differential vertical acceleration of parcels of different density (Dreeben and Kerstein, 2000). This setup might capture lateral entrainment driven by the buoyancy-induced horizontal shear, and thus might have some relevance to cumulus convection within a plume-modeling framework (Cheinet, 2003).

For use as a GCM near-surface closure, ODT has advantages that are not directly indicated by the application considered here. For example, ODT is an unsteady simulation with LES-like behaviors such as time-lagged response to transients, yet could be implemented affordably as a GCM closure. On the other hand, because it represents an instantaneous state rather than an ensemble, it cannot evolve useful ensemble properties such as cloud fraction. In these respects, ODT may be complementary to other methods, such that a judicious combination of methods may provide an optimal GCM closure solution, e.g., within the multiscale modeling framework that is currently under development.

ACKNOWLEDGEMENT

The authors would like to thank S. Krueger for his guidance and encouragement. This research was supported by the Division of Chemical Sciences, Geosciences, and Energy Biosciences, Office of Basic Energy Sciences, U.S. Department of Energy.

References

[1] Cheinet, S., 2003: A multiple mass-flux parameterization for the surface-generated convection. Part I, Dry plumes. *J. Atmos. Sci.*, **60**, 2313–2327.

[2] Cuxart, J., et al., 2004: Single-column intercomparison for a stably stratified atmospheric boundary layer. *Boundary Layer Meteorol.*, in press.

[3] Dreeben, T. D., and Kerstein, A. R., 2000: Simulation of vertical slot convection using one-dimensional turbulence. *Int. J. Heat Mass Transf.*, **43**, 3823–3834.

[4] Kerstein, A. R., 1991: Linear-eddy modeling of turbulent transport. Part 6. Microstructure of diffusive scalar mixing fields. *J. Fluid Mech.*, **231**, 361–394.

[5] Kerstein, A. R., 1999: One-dimensional turbulence, Formulation and application to homogeneous turbulence, shear flows, and buoyant stratified flows. *J. Fluid Mech.*, **392**, 277–334.

[6] Kerstein, A. R., 2002: One-dimensional turbulence, A new approach to high-fidelity subgrid closure of turbulent flow simulations. *Comp. Phys. Commun.*, **148**, 1–16.

[7] Kerstein, A. R., Ashurst, W. T., Wunsch, S., and Nilsen, V., 2001: One-dimensional turbulence, vector formulation and application to free shear flows. *J. Fluid Mech.*, **447**, 85–109.

[8] Kosovic, B., and Curry, J., 2000: A large eddy simulation study of a quasy-steady, stably stratified atmospheric boundary layer. *J. Atmos. Sci.*, **57**, 1052–1068.

[9] Moeng, C.-H., 1984: A large-eddy-simulation model for the study of planetary boundary layer turbulence. *J. Atmos. Sci.*, **41**, 2052–2062.

[10] Pope, S. B., 2000: *Turbulent Flows*. Cambridge University Press, Cambridge.

[11] Schmidt, R. C., Kerstein, A. R., Wunsch, S., and Nilsen, V., 2003: Near-wall LES closure based on one-dimensional turbulence modeling. *J. Comp. Phys.*, **186**, 317-355.

[12] Stevens, B., 2003: DYCOMS-II (RF01), http://www.atmos.ucla.edu/~bstevens/dycoms/dycoms.html.

[13] Stull, R. B., 1988: *An Introduction to Boundary Layer Meteorology*. Kluwer, Dordrecht.

[14] Su, C.-W., Krueger, S. K., McMurtry, P. A., and Austin, P. H., 1998: Linear eddy modeling of droplet spectral evolution during entrainment and mixing in cumulus clouds. *Atmos. Res.*, **47-48**, 41–58.

[15] Wunsch, S., 2003: Stochastic simulations of buoyancy-reversal experiments. *Phys. Fluids*, **15**, 1442-1456.

[16] Wunsch, S., and Kerstein, A. R., 2001: A model for layer formation in stably-stratified turbulence. *Phys. Fluids*, **13**, 702-712.